

Microelectromechanical scanning probe instruments for array architectures

Scott A. Miller^{a)}

School of Applied and Engineering Physics and the Cornell Nanofabrication Facility, Cornell University, Ithaca, New York 14853

Kimberly L. Turner

Department of Theoretical and Applied Mechanics and the Cornell Nanofabrication Facility, Cornell University, Ithaca, New York 14853

Noel C. MacDonald

School of Electrical Engineering and the Cornell Nanofabrication Facility, Cornell University, Ithaca, New York 14853

(Received 7 July 1997; accepted for publication 26 August 1997)

A compact ($150\ \mu\text{m} \times 150\ \mu\text{m}$), electrostatic actuator for out-of-plane (z) actuation of a probe tip has been designed, fabricated, and tested. Static deflections of $\pm 0.7\ \mu\text{m}$ out of the plane of the substrate have been achieved. The device consists of a single crystal silicon tip on a torsional cantilever with out-of-plane interdigitated electrode capacitors. This cantilever and electrode design allows a wide range of stiffnesses, actuator force, and frequency response. Significant improvements in performance (larger tip displacement and increased sense capacitance) and a higher density of devices per unit area can be obtained as the minimum feature size decreases. Applications such as information storage, molecular manipulation, and nanolithography require high density, parallel arrays for reasonable throughput. To demonstrate the suitability of this device for use in such arrays, a 12×12 array of microelectromechanical probe tips with integrated actuators and capacitive sensors for scanning probe microscopy has been fabricated. The size of each array element is about $150\ \mu\text{m}$ by $150\ \mu\text{m}$ with a tip-to-tip spacing in the array of $200\ \mu\text{m}$. Given these dimensions, the packing density of the devices is about $2500\ \text{units}/\text{cm}^2$. © 1997 American Institute of Physics. [S0034-6748(97)04711-4]

I. INTRODUCTION

Scanning probe microscopes have become important tools for analyzing surfaces at the μm and nm scales. Besides imaging, these instruments have been used to manipulate atoms on a surface, measure forces between atoms, and perform nanolithography.¹⁻⁴ Unfortunately, to utilize this capability for many applications such as data storage and nanolithography, an increase in throughput (operations per second) is required.

One approach to achieving higher throughput is to micromachine parallel probe structures. The throughput is increased by the simultaneous operation of many instruments: the more instruments operating, the greater the throughput. However, the large number of instruments should occupy a reasonable chip area. Therefore, for use in dense $n \times n$ array architectures of scanned probe instruments, a micromechanical device must be extremely compact, sense weak interactions, and achieve precision nm-scale motion to track surface topography. Massively parallel array architectures of scanned probe devices require the integration of small, low mass, high frequency cantilevers with tips. One major challenge is the detection of nm-scale vertical displacements of each cantilever without having an external beam of light and external detector for each cantilever. An additional challenge is to include the out-of-plane actuation of the tip to compensate for and to track variations in surface topography and slope.

Force sensing microcantilevers with integrated actuation have been constructed. The majority of these cantilevers use sputtered ZnO ⁵⁻⁷ and sol-gel derived lead zirconium titanate (PZT) thin films.^{8,9} Deposition and etching of these films require techniques not found in standard silicon very large scale integrated (VLSI) circuit fabrication. Poling of the films and the change in their behavior with temperature pose difficulties when using piezoelectric films. There are also several design disadvantages with these cantilevers. The cantilever must have at least three thin film layers (bottom electrode, piezoelectric, and top electrode). Each layer contributes to the stiffness of the cantilever. In addition, the piezoelectric film thickness has to be chosen to maximize the deflection of the cantilever for a given voltage across the film. If the piezoelectric film becomes too thick relative to the thickness of the cantilever, the applied voltage elongates the beam rather than bending it.⁶ All of these factors must be considered during the design of the cantilever. Different applications require different combinations of dimensions, materials, and layer thicknesses.⁸

Silicon micromachining technology without piezoelectric films has been used to produce force sensing cantilevers with actuation.¹⁰⁻¹² These cantilevers rely on parallel plate electrodes to provide an electrostatic force for actuation as well as a capacitance for deflection sensing. As the device size is scaled downward, however, the area of the electrodes decreases. This results in less actuation force and less sensing capacitance.

The research presented here focuses on developing microelectromechanical scanning probe instruments for array

^{a)}Electronic mail: sam8@cornell.edu

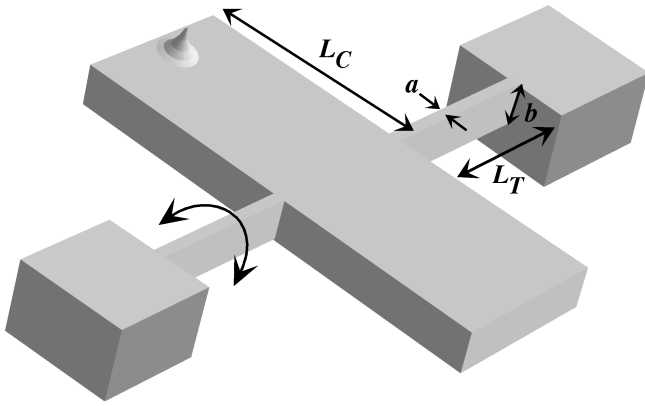


FIG. 1. A torsional cantilever consists of a rigid plate mounted on two support beams about which it can rotate.

architectures with an emphasis on scaling laws. Consequently, our design is composed of a silicon torsional cantilever with high aspect ratio, out-of-plane interdigitated electrodes for capacitance-based detection and actuation. The device's behavior depends on independent, lithography-based parameters that can be scaled easily. Improved performance is obtained as the device size and the minimum feature size (MFS) are scaled downward. The design is extremely flexible and allows us, for example, to change the actuation force without affecting the cantilever's frequency response and stiffness.

II. DEVICE DESIGN ANALYSIS

A. Torsional cantilever

For many years, torsion has been used as a sensitive technique for measuring force interactions; examples include Coulomb's torsional balance for electrostatic forces and Cavendish's balance for gravitational forces. A torsional cantilever is a rigid plate supported by two beams about which it can rotate, such as shown in Fig. 1. A detailed analysis of the torsional cantilever has been previously reported.¹³ The torsional rigidity, k_θ , of the cantilever with support beams of rectangular cross section is defined as¹⁴

$$k_\theta \equiv \frac{T}{\theta} = 2\beta G \frac{a^3 b}{L_T}, \quad (1)$$

where T is the torque, θ is the angle of rotation about the central axis, a is the width of the torsional support beams, b is the height of the beams, L_T is the length of one support beam, G is the shear modulus of rigidity of the material [$G = 7.96 \times 10^{10}$ N/m² for Si(100)],¹⁵ and $\beta (\cong \frac{1}{3})$ is a constant determined by the aspect ratio b/a .

When a force, F_z , acts on the cantilever a distance L_C from the torsional supports, the torque experienced by the cantilever is

$$T = F_z L_C. \quad (2)$$

The angle of rotation, θ , of the cantilever is then the deflection of one end of the cantilever, Δz , divided by the distance from the torsional supports to the end of the cantilever (i.e., the length of the cantilever)

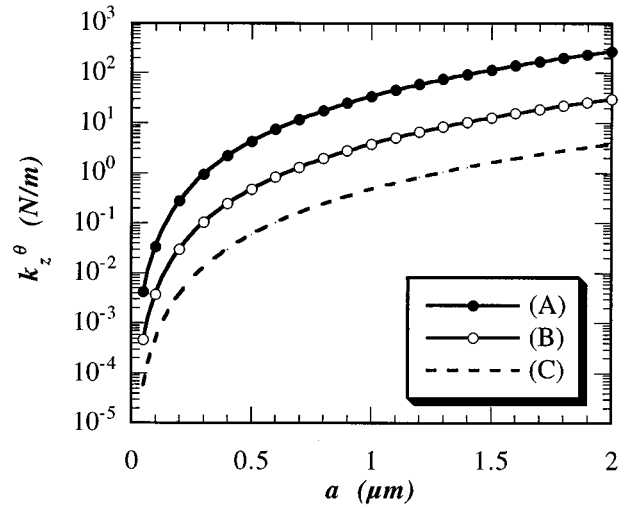


FIG. 2. The effective out-of-plane spring constant (k_z^θ) of a torsional cantilever as a function of the support beam width (a). The three curves are plotted for $b = 10 \mu\text{m}$ and (A) $L_T = 25 \mu\text{m}$, $L_C = 25 \mu\text{m}$; (B) $L_T = 25 \mu\text{m}$, $L_C = 75 \mu\text{m}$; and (C) $L_T = 50 \mu\text{m}$, $L_C = 150 \mu\text{m}$.

$$\theta = \frac{\Delta z}{L_C}. \quad (3)$$

Therefore, by substituting Eqs. (2) and (3) into Eq. (1), we can define the effective spring constant k_z^θ of the torsional cantilever as

$$k_z^\theta \equiv \frac{F_z}{\Delta z} = 2\beta G \frac{a^3 b}{L_C^2 L_T}. \quad (4)$$

Figure 2 shows the range of k_z^θ as a function of the geometric variables a , L_T , and L_C . These plots show that torsional cantilevers of a reasonable size for array architectures can achieve spring constants between 10^{+2} and 10^{-4} N/m. Higher spring constants ($> 10^{+2}$ N/m) can be made by having shorter cantilever lengths or additional torsional supports. Because of the high aspect ratio (b/a) of the beams, the beams exhibit no curling or buckling. Any non-planarity of the cantilever due to thermal or intrinsic stress can be controlled by the proper choice of processing parameters.¹⁶

Theoretically, the following simple relation gives an accurate estimation of the resonant frequency:

$$f_0 = \frac{1}{2\pi} \sqrt{\frac{k_\theta}{I_\theta}}, \quad (5)$$

where k_θ is the torsional rigidity and I_θ is the moment of inertia. Since the geometry and materials for the torsional cantilever are known, a fairly accurate estimation of I_θ can be made. Consequently, experimental measurement of the resonant frequency allows us to determine the stiffness of the cantilever. A more complete analysis of the dynamics of this system is performed elsewhere.¹⁷ There is a tradeoff between the frequency response of the cantilever and its displacement. As Eq. (5) shows, to increase the frequency of the cantilever the stiffness has to increase or the moment (mass) has to decrease. Increasing k_θ is accomplished by adjusting the parameters in Eq. (1) (i.e., a , b , and L_T). For a given

force, however, the deflection of the cantilever decreases with increasing stiffness. Decreasing the mass of the cantilever involves decreasing parameters such as L_C , b , and the chip area of the device. As will be shown below, decreasing these parameters results in less actuation force and less cantilever deflection. Since all of these parameters, except b which is defined by an etch step, are defined by lithography, the cantilever design can be optimized for the desired frequency response and the maximum deflection. Deflection range may be reduced to increase frequency response or vice versa. In an array architecture, the frequency response of each cantilever may be sacrificed to increase deflection range since throughput (operations per second) is increased by the parallel operation of many instruments.

The torsional cantilever is ideally suited for a force balance technique.¹⁸ The advantages of force balance include improved overall linearity, a controllable spring constant, a mechanically balanced system immune to gravitational and inertial effects, and, in closed loop operation, the structure moves very little (reduced air damping and short response time).

B. Electrodes

1. Capacitive sensing of cantilever deflection

For sensing torsional deflections, capacitive electrodes are integrated on the same chip as the torsional cantilever. The microfabrication of the cantilever, tip, and electrodes on the same chip eliminates many of the asymmetries which result from hand assembly of torsional cantilevers. Instead of the typical parallel plate capacitor configuration to sense out-of-plane deflections of the cantilever,¹⁰⁻¹² we have chosen to use an out-of-the-plane, interdigitated electrode design. There are several advantages of this design. Since this device does not use the substrate as one plate of a parallel plate capacitor, there is no need for patterning electrodes underneath the released structure. More importantly, however, the interdigitated electrode capacitors can provide substantially more capacitance per unit chip area of silicon than a parallel plate configuration.

A parallel plate capacitor has a capacitance per unit chip area, c_{pp} , of

$$c_{pp} = \frac{\epsilon_0}{d}, \quad (6)$$

where d is the gap between the movable plate and the substrate.

The interdigitated electrode design is shown in Fig. 3. Each unit occupies a chip area of

$$A_{\text{unit}} = (2l_p + 4a')(2a' + 2d') = 4(l_p + 2a')(a' + d'), \quad (7)$$

where a' is the width of the electrode, l_p is the length of the electrode, and d' is the gap between electrodes.

The number of interdigitated electrode units in a given chip area of silicon (A) is

$$N_{\text{unit}} = \frac{A}{4(l_p + 2a')(a' + d')}. \quad (8)$$

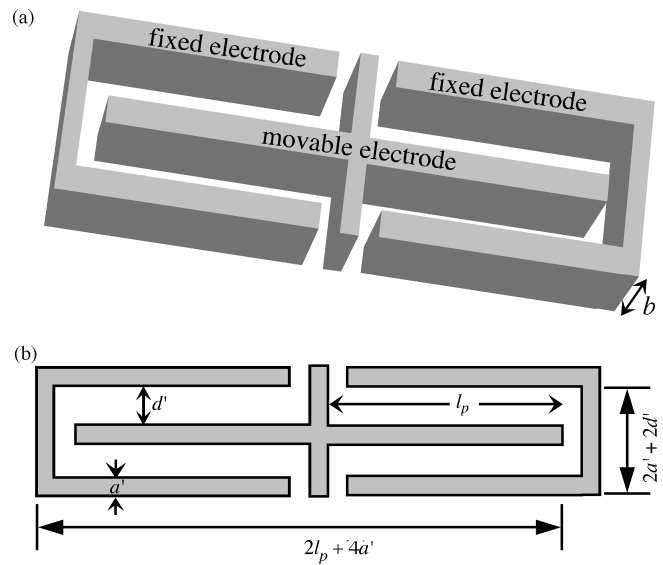


FIG. 3. A diagram of the interdigitated electrode capacitor. (a) The interdigitated electrode capacitor consists of two fixed electrodes surrounding a central electrode which is free to move in and out of the plane of the substrate. (b) A top down view of an interdigitated capacitor unit showing the dimensions and area of one unit.

The capacitance of each interdigitated electrode unit is

$$c_{\text{unit}} = 4 \frac{\epsilon_0(l_p - a')b}{d'}, \quad (9)$$

where b is the height of the electrodes out of the plane of the substrate. Combining Eqs. (8) and (9) and assuming $l_p \gg a'$, we arrive at the capacitance per unit chip area, c_{ic} , for the interdigitated electrode capacitor

$$c_{ic} = \frac{\epsilon_0 b}{d'(a' + d')} = \frac{b}{(a' + d')} c_{pp}, \quad (10)$$

where $d' = d$. If the gap is the same width as the electrode ($d' = a'$), then the capacitance per unit chip area is

$$c_{ic} = \frac{1}{2} \left(\frac{b}{a'} \right) c_{pp}. \quad (11)$$

The *aspect ratio* of the interdigitated electrodes determines the difference in the capacitance per unit chip area between the interdigitated electrode capacitor and the parallel plate capacitor, i.e., the higher the aspect ratio of the interdigitated electrodes, the greater their capacitance per unit chip area of silicon. Typical aspect ratios for our devices range between 10:1 and 20:1. With the development of deep silicon plasma etchers, these aspect ratios should approach 100:1. When scaling down the size (chip area) of the devices, the capacitance of the parallel plate electrodes decreases. With the interdigitated electrode configuration, the aspect ratio provides an independent parameter which can be adjusted to compensate for the decrease in area.

2. Capacitive actuation of the cantilever

Capacitors not only provide the means for sensing deflections of the cantilever, but also supply the electrostatic

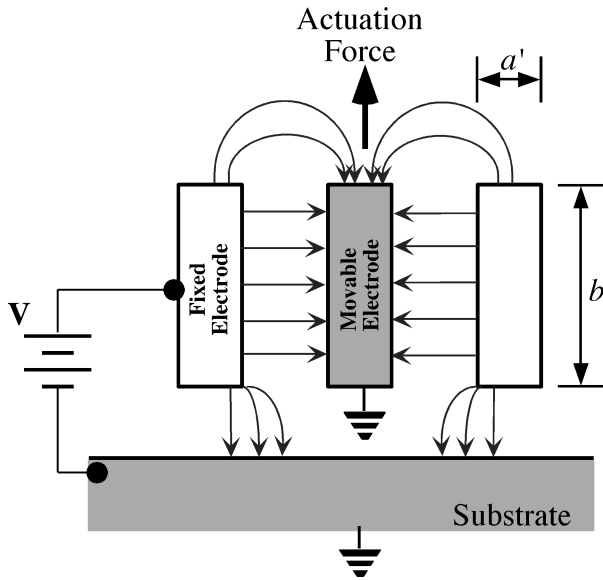


FIG. 4. The electric field lines between the electrodes and the substrate. The asymmetric field distribution results in the out-of-plane actuation force.

force for actuation in the out-of-plane direction. The parallel plate configuration yields an electrostatic force per unit area of¹²

$$f_{pp} = \frac{1}{2} \epsilon_0 \frac{V^2}{d^2} = \frac{1}{2} \frac{c_{pp}}{d} V^2. \quad (12)$$

The static deflection is found by equating the spring restoring force to the electrostatic force. When the static deflection reaches $d/3$, the electrostatic force exceeds the spring restoring force and the cantilever “snaps” to the substrate electrode.

The interdigitated electrode capacitive actuators take advantage of the electrostatic comb drive levitation effect.¹⁹ The substrate and movable electrodes are grounded while a potential is applied to the fixed electrodes. The vertically asymmetric electric field acting on the movable electrodes results in a vertical force (Fig. 4). This force levitates the movable electrodes away from the substrate. We use this force to cause static displacements or vibrational excitations of the cantilever. A simulation of this force was performed for the geometry of our device and the resulting torque as a function of angular displacement of the cantilever is shown in Fig. 5. The region of interest is the approximately linear region around $T_{lev}=0$. It is approximated by

$$T_{lev} = \gamma_\theta V^2 \left(\frac{\theta_0 - \theta}{\theta_0} \right), \quad (13)$$

where V is the potential applied to the fixed electrodes, θ_0 is the angle at which $T_{lev}=0$, and γ_θ is the drive capacity.

The total torque acting on the cantilever includes the levitation torque provided by the interdigitated electrodes and the passive restoring torque provided by the torsional supports. The static deflection of the cantilever is then found by solving

$$T_{net} = T_{lev} - T_{spring}, \quad (14)$$

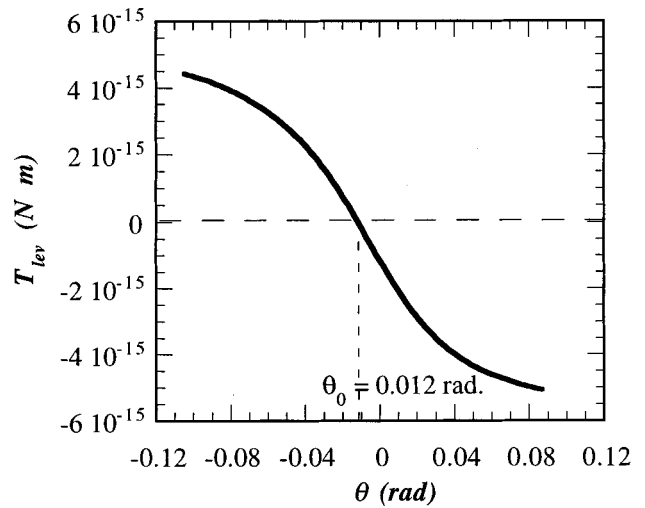


FIG. 5. A plot of the levitation torque as a function of angle. The equilibrium position occurs at $\theta_0=0.012$ rad as indicated.

where T_{net} is the net torque acting on the cantilever and T_{spring} is the restoring torque provided by the torsional supports. With $T_{spring} = k_\theta \theta$, we substitute Eqs. (1) and (13) into Eq. (14), solve for θ , and obtain

$$\theta = \frac{\gamma_\theta V^2 \theta_0}{k_\theta \theta_0 + \gamma_\theta V^2}. \quad (15)$$

The tip of the cantilever is located a distance L_C from the axis of rotation. Therefore, the static z deflection of the tip is given by

$$z \approx L_C \theta = \frac{\gamma_\theta V^2 \theta_0 L_C}{k_\theta \theta_0 + \gamma_\theta V^2}. \quad (16)$$

C. Scaling

Our design was chosen for several reasons. First and most important, as seen in Eq. (1), the torsional stiffness scales as a^3 , where a is the width of the torsional support beam. This width is defined by the MFS of the lithography. Thus, as the MFS decreases, the cantilever becomes less rigid and easier to deflect with a smaller force. Its sensitivity to weaker forces is subsequently increased. Figure 2 illustrates this scaling of stiffness with torsional support beam width (a). Second, the design uses compact, high aspect ratio interdigitated capacitors moving in and out of the plane for sensing deflections of the cantilever. As seen in Eq. (11), because of their high aspect ratio, the interdigitated electrodes provide more capacitance per unit chip area of silicon than parallel plate capacitors. As the electrode width (a') and the gap (d') are scaled downward, more capacitor plates can occupy a given chip area A [Eq. (8)], increasing the capacitance for sensing. Moreover, these capacitors also supply the force for actuation in the out-of-plane direction. The greater the number of electrodes, the larger the drive capacity, γ_θ , and the larger the levitation torque [Eq. (13)]. As an example, we assume a cantilever with $L_C = 75 \mu\text{m}$, $d' = 2 \mu\text{m}$, and $a' = 1 \mu\text{m}$. With a stiffness $k_\theta = 1.6 \times 10^{-9} \text{ N m/rad}$ and $\gamma_\theta = 7.6 \times 10^{-14} \text{ N m/N}^2$, Eq. (16) yields $0.55 \mu\text{m}$ for $V = 20 \text{ V}$. When we scale a' to $0.5 \mu\text{m}$

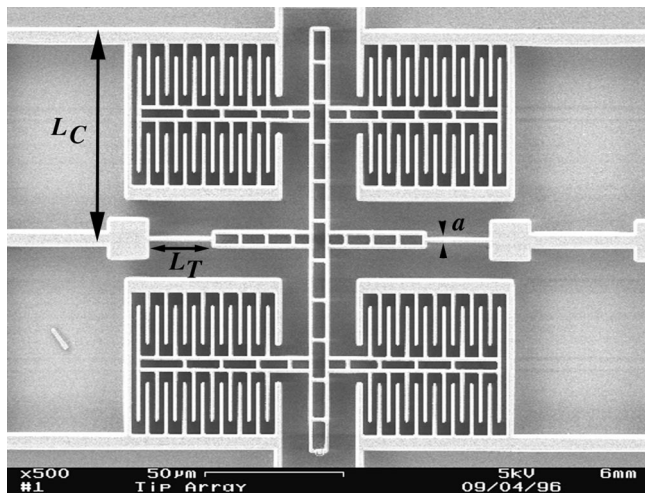


FIG. 6. A top view of one of the torsional cantilever designs. For this device, $L_C=80 \mu\text{m}$, $L_T=25 \mu\text{m}$, and $a=1 \mu\text{m}$.

and d' to $1 \mu\text{m}$, the cantilever achieves $0.68 \mu\text{m}$ of out-of-plane deflection for $V=20 \text{ V}$. There is no change in the stiffness or the mass (i.e., frequency response and force sensitivity) of the cantilever. There is, however, a 23% increase in the out-of-plane static deflection and a fourfold increase in total sense capacitance. Combining a reduction in stiffness with the increase in force produces a larger displacement per applied voltage [Eq. (16)].

Scaling the size of the torsional cantilever also allows for a higher density of devices per unit chip area. The higher density generates an increase in throughput by the operation of more units and by the reduction in the xy scan range requirements for the system. The present device density is $2500 \text{ elements/cm}^2$.

III. EXPERIMENTAL RESULTS

A. Fabrication

Using the design ideas expressed above, a microelectromechanical probe tip with integrated actuators and capacitive sensors for scanning probe microscopy was fabricated (Fig. 6). Each array element consists of a single crystal silicon tip (Fig. 7) on a torsional cantilever with out-of-plane interdigitated electrode capacitors.

The arrays were fabricated using a modification of the single crystal reactive etch and metallization (SCREAM) silicon micromachining process.^{20,21} This fabrication process allows us to integrate tips onto torsional cantilevers using only three masks or lithographic steps. The fabrication of the device starts with a single crystal silicon (100) wafer. The wafer is oxidized (wet, $1100 \text{ }^\circ\text{C}$) to produce $0.4\text{--}0.5 \mu\text{m}$ of silicon dioxide. The first mask and photolithography step defines $0.4\text{-}\mu\text{m}$ -diam circles at the tip locations. The pattern is then etched into the mask oxide via a CHF_3 reactive ion etch (RIE) [Fig. 8(a)]. After stripping photoresist, a chlorine RIE etches $3\text{-}\mu\text{m}$ -high columns into the silicon using the thermal oxide as a mask [Fig. 8(b)]. A second thermal oxidation (wet, $1100 \text{ }^\circ\text{C}$) is performed to oxidize through the silicon columns. This forms the silicon tip at the base of the oxidized column [Fig. 8(c)]. An anisotropic etch (CHF_3 RIE) of

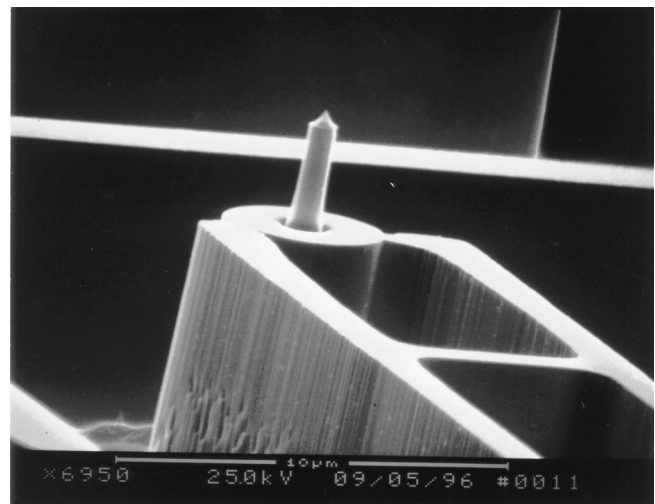


FIG. 7. A closeup of the single crystal silicon tip integrated onto the end of the torsional cantilever.

the oxide is done [Fig. 8(d)], immediately followed by a $5\text{--}6 \mu\text{m}$ deep silicon (Cl_2 RIE) etch to form the tip shaft [Fig. 8(e)]. A $2.5 \mu\text{m}$ silicon oxide layer is deposited using plasma enhanced chemical vapor deposition [Fig. 8(f)]. A second mask is used to define the actuator and perform standard SCREAM.²⁰ At the end of the SCREAM process, the device is essentially complete except the tip and torsional supports are covered by oxide and metal. To remove these materials, a

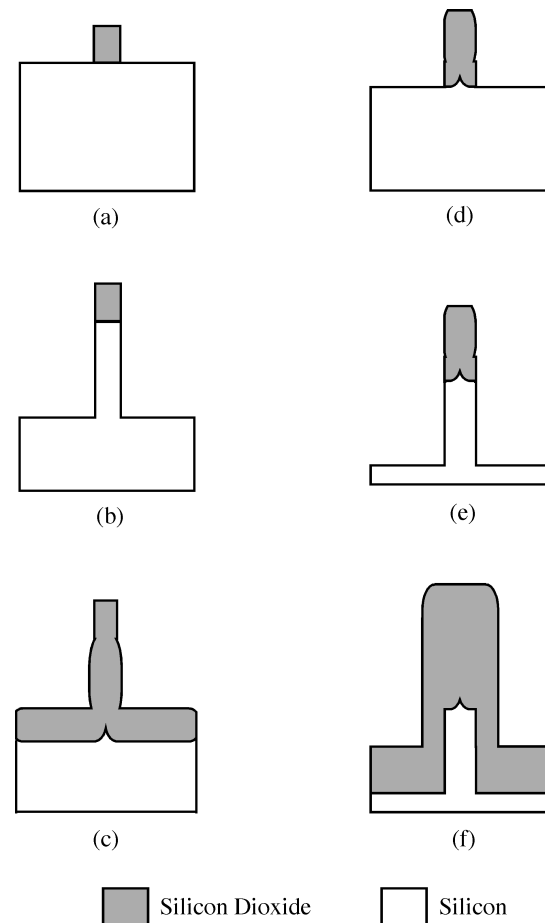


FIG. 8. The tip fabrication process.

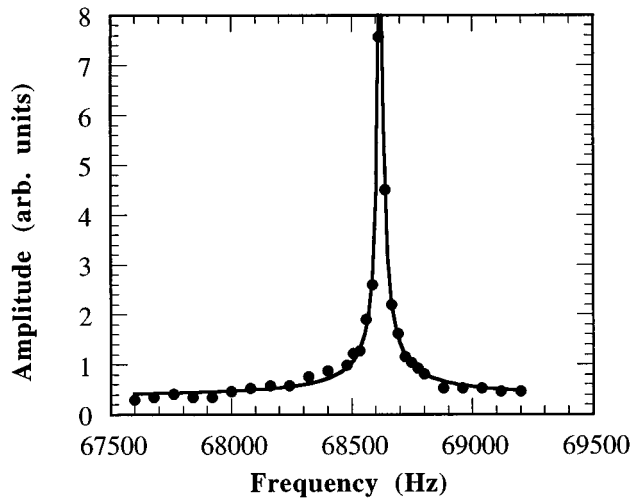


FIG. 9. Frequency response of a torsional cantilever as measured in the SEM.

thick photoresist (AZP-4903) is spun onto the wafer and a third mask is used to expose an area around the tip and support beams. An aluminum etch and a buffered oxide etch are then done. The thick photoresist is then removed and the fabrication process is complete.

B. Mechanical behavior

Mechanical testing of the torsional cantilever is performed under scanning electron microscope (SEM) observation. The dynamic behavior of the torsional cantilevers, which can be modeled with the Mathieu equation, is analyzed. A more detailed analysis of the dynamics of this system will be presented elsewhere.¹⁷ From SEM observation, we recorded the amplitude of vibration as a function of the applied driving frequency. The result of our measurement is shown in Fig. 9. The resonant frequency of the cantilever is 68.6 kHz.

For mechanical measurements in air, a method for capacitive measurement of the microstructure's oscillation is used. Theoretically, the capacitance is about 2×10^{-14} F. The signal generated by the motion can be extracted from the cross talk signal using frequency-selective electronics. A sinusoidal voltage signal at frequency f is applied only to the interdigitated electrodes on one side of the torsional cantilever, e.g., the electrodes in the upper half of Fig. 6. As a consequence of the force-voltage relation for electrostatic actuation [Eq. (13)], the structure oscillates at frequency $2f$. The structure's motion creates a changing sense capacitance in the second set of interdigitated electrodes on the other side of the torsional cantilever. Cross talk between the driving and sensing signals is subsequently reduced since the resulting motion signal is at frequency $2f$, not the drive frequency f . After preamplification, this motion signal is measured using a lock-in amplifier with its reference frequency at twice the driving frequency. Output of the lock-in as the frequency was swept is shown in Fig. 10. From this data and the curve fit of Eq. (15), the resonant frequency of the cantilever is found to be 69 kHz. Operation in air, however, introduces a significant amount of damping to the system.

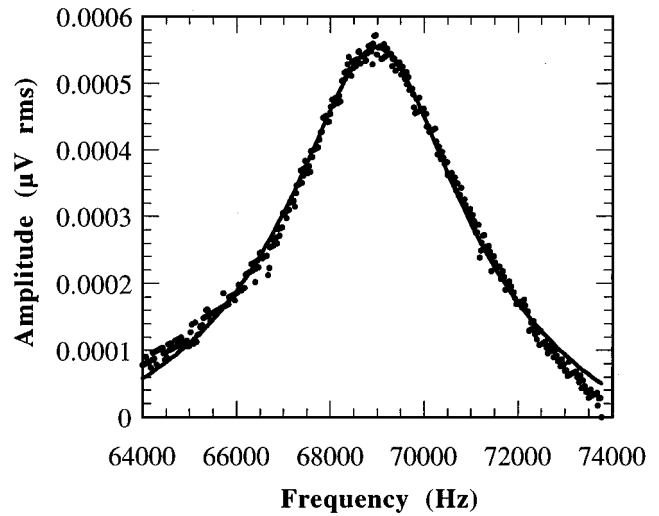


FIG. 10. Frequency response of the torsional cantilever as measured in air.

A second set of torsional cantilevers was fabricated to investigate the effects of scaling. These cantilevers are identical to that shown in Fig. 6 except the width (a) of the torsional supports was varied. The frequency response of these cantilevers was tested in the SEM and the results are presented in Table I.

In addition to the dynamic response of the torsional cantilevers, we have measured the out-of-plane static deflection under SEM observation. The results of this measurement are shown in Fig. 11. The curves shown on the plot are actually the theoretical curves generated by Eq. (16). The parameters for the $a=1 \mu\text{m}$ torsional cantilever are: $\theta_0=0.019$ rad, $\gamma_\theta=7.86 \times 10^{-14}$ N m/V², and $k_\theta=1.88 \times 10^{-8}$ N m/rad. For the $a=0.5 \mu\text{m}$ cantilever the parameters are: $\theta_0=0.011$ rad, $\gamma_\theta=7.56 \times 10^{-14}$ N m/V², and $k_\theta=1.64 \times 10^{-9}$ N m/rad.

Figure 11 displays the effects of scaling the width (a) of the torsional support beams. Both static response curves indicate that $0.7 \mu\text{m}$ of out-of-plane deflection can be achieved when using one set of fixed electrodes. Using both sets of electrodes, the total range of deflection is $\pm 0.7 \mu\text{m}$. However, the voltage necessary to obtain such a deflection is about 30 V for the device with $a=0.50 \mu\text{m}$ and about 70 V for the device with $a=1 \mu\text{m}$. Since the width (a') and gap (d') of the interdigitated electrodes were not scaled, the drive capacity (γ_θ) remained constant as the curve fit parameters show. Only the torsional stiffness of the cantilevers was scaled. The curve fit values can be compared to those obtained theoretically in Table I. The values exhibit reasonable agreement and we did observe approximately an order of magnitude decrease in stiffness as the torsional support

TABLE I. Experimental measurements of cantilever properties ($b=7 \mu\text{m}$, $L_T=25 \mu\text{m}$, $L_C=80 \mu\text{m}$).

a (μm)	k_θ theory (N m/rad)	f_0 theory (kHz)	f_0 meas (kHz)
1	1.52×10^{-8}	56.5	56.8
0.75	6.40×10^{-9}	36.7	39.9
0.50	1.90×10^{-9}	20.0	22.8

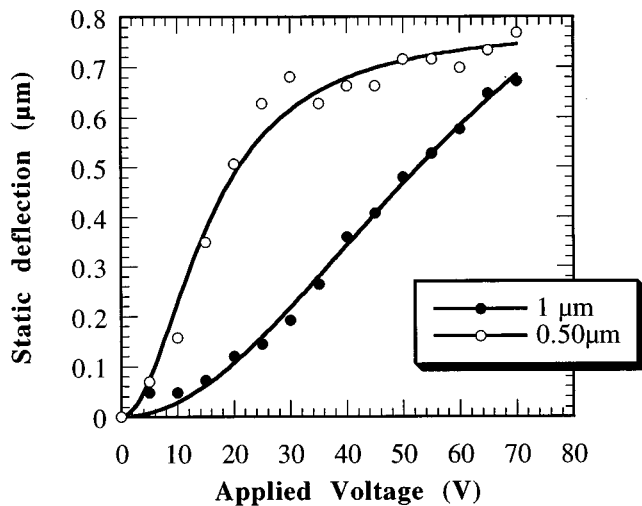


FIG. 11. Static deflection of the torsional cantilever array elements as a function of applied voltage. The data shown are for elements identical to that shown in Fig. 8 with $a = 1 \mu\text{m}$ and $a = 0.50 \mu\text{m}$.

width was scaled downward by a factor of 1/2. Sources of error are attributed to inaccurate dimensional measurements and the possibility that the film coatings were not entirely removed from the torsional supports.

C. Force sensing

The cantilever has been used to sense a force interaction. In air, a conductive tip was approached toward the cantilever, brought into contact, and retracted. The change in capacitance between the fixed electrodes and the movable electrodes was recorded using an HP 4274A LCR meter. The results of this measurement are shown in Fig. 12. The relatively large “jumps” in capacitance clearly indicate the hysteresis expected from an attractive capillary force. The magnitude of the change is due in part to the change in conductive area when the tip contacts the cantilever. From the amount of cantilever deflection during tip retraction ($\sim 1.2 \mu\text{m}$) and the effective stiffness of the cantilever ($\sim 0.1 \text{ N/m}$), we estimate the capillary force as 1.2

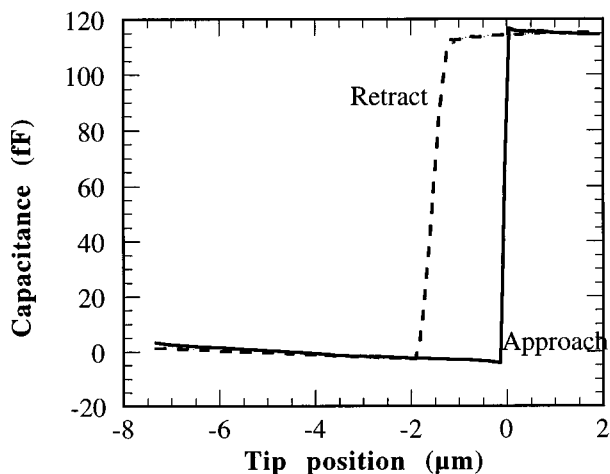


FIG. 12. The capacitance between the fixed and movable electrodes of the torsional cantilever when a conductive tip is approached and retracted.

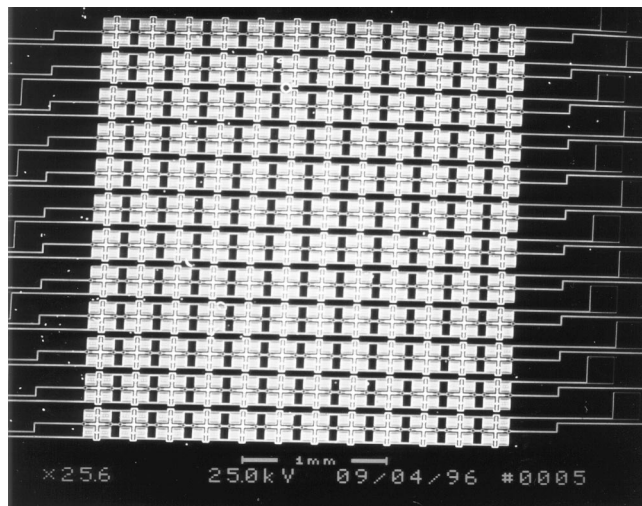


FIG. 13. A 12×12 array of torsional cantilevers with integrated tips. The entire array occupies an area of $2.4 \text{ mm} \times 2.4 \text{ mm}$.

$\times 10^{-7} \text{ N}$. This value compares favorably with the $10^{-8} - 10^{-7} \text{ N}$ typically observed in atomic force microscopy in air.²² For nN force detection with this particular cantilever, fF sensitivity is needed and requires a bandwidth less than 50 kHz. The integrated wires produce a parasitic capacitance of about 1 pF in parallel with the sense capacitance. With modern phase locked loops we achieve signal to noise ratios on the order of $10^1 - 10^2$. The parasitic capacitance can be reduced by a few orders of magnitude by integrating electronics on chip. In addition, the sense capacitance can be substantially increased by scaling the parameters a' , d' , and b [Eq. (10)].

IV. ARRAY ARCHITECTURES

To demonstrate the suitability of this device for use in scanning probe arrays, we have fabricated arrays (2×2 up to 12×12) of microelectromechanical probe tips with integrated actuators and capacitive sensors for scanning probe microscopy. An example of one array is shown in Fig. 13. The array elements are identical to the device shown in Fig. 6 with a tip-to-tip spacing in the array of $200 \mu\text{m}$. The packing density of the devices is about 2500 units/cm^2 .

While this array did not include circuitry for the independent sensing and deflection of each cantilever, methods exist to integrate electronic circuits with the micromechanical cantilevers. For low density arrays, each array element can be fabricated adjacent to prefabricated integrated circuits for signal preamplification.²³ As the arrays become more dense, other methods such as through-wafer contacts to integrated circuits and integration of active devices into the micromechanical structures²⁴ become necessary to achieve high packing densities. Signal preamplification will significantly reduce the difficulties of noise and cross talk between adjacent cantilevers.

ACKNOWLEDGMENTS

This work is supported by DARPA and an instrumentation grant from the NSF. One of the authors (K.L.T.) would

like to acknowledge the fellowship support of the NSF. All microfabrication was performed at the Cornell Nanofabrication Facility which is supported by the NSF, Cornell University, and Industrial Affiliates. The authors would like to thank the CNF staff for their assistance. The authors would also like to thank Scott Adams and M. Taher Saif for useful discussions on mechanics and Peter Hartwell and Fred Bertsch for their technical assistance.

- ¹R. Wiesendanger, *Scanning Probe Microscopy and Spectroscopy* (Cambridge University Press, Cambridge, 1994).
- ²*Scanning Tunneling Microscopy*, edited by J. A. Strosio and W. J. Kaiser (Academic, Boston, 1993).
- ³D. M. Eigler and E. K. Schweizer, *Nature* (London) **344**, 524 (1990).
- ⁴*Technology of Proximal Probe Lithography*, edited by C. R. K. Marrian (SPIE, Bellingham, Washington, 1993).
- ⁵T. R. Albrecht, S. Akamine, M. J. Zdeblick, and C. F. Quate, *J. Vac. Sci. Technol. A* **8**, 317 (1990).
- ⁶S. C. Minne, S. R. Manalis, and C. F. Quate, *Appl. Phys. Lett.* **67**, 3918 (1995).
- ⁷T. Itoh, T. Ohashi, and T. Suga, *MEMS'96, Proceedings of the 9th International Workshop on MicroElectroMechanical Systems* (IEEE, Piscataway, 1996), p. 451.
- ⁸C. Lee, T. Itoh, R. Maeda, and T. Suga, *Rev. Sci. Instrum.* **68**, 2091 (1997).
- ⁹T. Itoh, C. Lee, J. Chu, and T. Suga, *MEMS'97, Proceedings of the 10th*

- International Workshop on MicroElectroMechanical Systems* (IEEE, Piscataway, 1997), p. 78.
- ¹⁰L. C. Kong, B. G. Orr, and K. D. Wise, *J. Vac. Sci. Technol. B* **11**, 634 (1993).
- ¹¹J. Bay, S. Bouwstra, E. Loegsgaard, and O. Hansen, *J. Micromech. Microeng.* **5**, 161 (1995).
- ¹²N. Blanc, J. Brugger, N. F. de Rooij, and U. Durig, *J. Vac. Sci. Technol. B* **14**, 901 (1996).
- ¹³S. A. Miller, Y. Xu, and N. C. MacDonald, *Proc. SPIE* **2640**, 45 (1995).
- ¹⁴S. P. Timoshenko and J. N. Goodier, *Theory of Elasticity* (McGraw-Hill, London, 1982), Chap. 10.
- ¹⁵J. J. Wortman and R. A. Evans, *J. Appl. Phys.* **36**, 153 (1965).
- ¹⁶M. T. A. Saif and N. C. MacDonald, *J. Microelectromechanical Sys.* **5**, 79 (1996).
- ¹⁷K. L. Turner, S. A. Miller, and N. C. MacDonald (in preparation).
- ¹⁸G. L. Miller, J. E. Griffith, E. R. Wagner, and D. A. Grigg, *Rev. Sci. Instrum.* **62**, 705 (1991).
- ¹⁹W. C. Tang, M. G. Lim, and R. T. Howe, *J. Microelectromechanical Sys.* **1** 170 (1992).
- ²⁰K. A. Shaw, Z. L. Zhang, and N. C. MacDonald, *Sens. Actuators A* **40**, 63 (1994).
- ²¹N. C. MacDonald, *Microelectron. Eng.* **32**, 49 (1996).
- ²²A. L. Weisenhorn, P. K. Hansma, T. R. Albrecht, and C. F. Quate, *Appl. Phys. Lett.* **54**, 2651 (1989).
- ²³K. A. Shaw and N. C. MacDonald, in Ref. 7, p. 44.
- ²⁴J. J. Yao, S. C. Arney, and N. C. MacDonald, *Sens. Actuators A* **40**, 77 (1994).